Article

Diagnosis and Control of Brown Leaf Spot of Kiwi (*Actinidia deliciosa*) Using Biochar-Zinc Oxide Nanocomposite (MB-ZnO) as a Non-Toxic Bio-Fungicides

Asif Kamal [1], Musrat Ali [1], Dunia A. Al Farraj [2], Enshad M. Al-Zaidi [2], Maria Khizar [1], Reem Amer Aljaaidi [2], Mohmed S. Elshikh [2] and Muhammad Farooq Hussain Munis [1,*]

[1] Department of Plant Sciences, Faculty of Biological Sciences, Quaid-i-Azam University, Islamabad 45320, Pakistan
[2] Department of Botany and Microbiology, College of Science, King Saud University, P.O. Box 2455, Riyadh 11451, Saudi Arabia
* Correspondence: munis@qau.edu.pk

Abstract: Kiwi is one of the best natural sources of vitamin C and has wide applications. During October–November 2021, small brown spots were examined on the Kiwi leaves. The diseased leaf samples were collected and placed on potato dextrose agar nutrient media for diagnosis. Morphological, anatomical, and molecular studies revealed this disease-causing agent to be *Rhizopus oryzae*. Molecular characterizations of the isolated pathogen were performed by using actin translation elongation factor (EF-1α) and ribosomal deoxyribose nucleotide inter transcribed sequence (rDNA ITS ITS1/ITS4) and elongation factors (EFl-F/EFl-R) primers. A BLAST study of the resultant ITS1/ITS4 sequence showed > 99% resemblance with *R. oryzae* (MT603964.1), while the EF-1α sequence revealed 100% similarity with translation elongation factor-1α gene of *R. oryzae* (MK510718.1). The obtained ITS1/ITS4 sequence was submitted to NCBI (MW603842.1). Koch's postulates established the pathogenicity of isolated *R. oryzae* and proved it to be the brown spot pathogen of Kiwi. For the environmentally-friendly management of Kiwi leaf spot, maize biochar-Zinc Oxide (MB-ZnO) nanocomposite was used. The prepared nanocomposite was characterized by Fourier transform infrared (FTIR) spectroscopy, thermo gravitational analysis (TGA), X-ray diffraction (XRD) analysis, scanning electron microscopy (SEM), and energy dispersive X-ray (EDX) analysis. After successful preparation, MB-ZnO was assessed for its possible antifungal potential against *R. oryzae*. MB-ZnO displayed substantial growth inhibition, and the highest growth inhibition (79%) was observed at a 19 mg/mL dose rate of nanoparticles. These excellent findings propose that Ball-milled synthesis is a fast, economical, and environmentally friendly method for nanocomposite in the near future. The nanocomposite is used as a nominal substitute for chemical fungicides.

Keywords: *Rhizopus oryzae*; Kiwi; ITS region; EF-1α gene; MB-ZnO

1. Introduction

Kiwi (*Actinidia chinensis*) is a perennial vine, and it is usually known by several other names, such as Chinese gooseberry, monkey peach, and sheep peach. Kiwi contains more "Vitamin C" than citrus and is delightful in taste. In the 1950s, Kiwi was first introduced in New Zealand [1]. In recent times, Italy has been the leading Kiwi-producing country (415,877 tons yield); second on the list is New Zealand (378,500 tons production) [2]. Other countries, such as Japan, Iran, Canada, France, Chile, and the USA also produce Kiwis in a great amount. Because of its distinct flavor and high nutritional value, efforts are being made to increase Kiwi production and its utilization in various traditional medicines [3,4]. Its different plant parts, including the root, stem, and leaves contain different health-friendly bioactive compounds [5]. More than 70 species of Kiwi have been grown in the world. Kiwi is considered a tropical plant as it has no tolerance to lower than 10 °C temperature [5].

Due to its potential role in human health, the biochemical properties of Kiwi have been extensively studied [6]. Studies reveal that A. deliciosa contains polyphenols, triterpenoids, polysaccharides, amino acids, vitamins, carotenoids, essential oils, and microelements [7]. It also contains a wide range of biologically active compounds that have been reported to have a curative part in tumors, inflammation, immunity, diabetes, and different heart diseases [8]. Additionally, the Kiwi can be used in the green synthesis of nanoparticles [9,10].

This study has characterized *Rhizopus oryzae*, which is a well-known plant pathogen. Over several decades, the classification and evolutionary study of the genus Rhizopus have been described. Based on the morphological features, Schipper and many others classified Rhizopus in detail [11,12]. Few scientists have also classified them based on their phylogenetic analyses [13]. The genus Rhizopus has been re-classified into 10 species and 7 varieties [14]. Over time, the study of phylogenetic relationships got better, and scientists started analyzing the phylogeny of other genes, such as actin (act1), translation elongation factor 1 α (EF-1α), and rDNA ITS [15]. *R. oryzae* is cosmopolitan in nature, and few studies have described it as a synonym of *R. arrhizus* [11]. *R. oryzae* belongs to the phylum Zygomycetes and causes significant yield losses [16]. It has been reported to cause infections in economically important crops, including Oryza sativa [17], Citrus medica [18], Ipomoea batatas [19], Cascabela thevetia [20], and Brassica campestris [21]. *R. oryzae* exists worldwide and appears in the form of white to gray mycelia, with several spores generating sporangia [22].

Plants are the main source of food, medicines, fiber, fodder, and other useful products for human beings. Plants are susceptible to various plant pathogens; among these, the fungus is the most common and damaging pathogen. Different kinds of carbonates, bicarbonates, sorbates, chelates, and silicates are used to treat fungal diseases [23]. These chemical fungicides are expensive and dangerously cause soil and water environmental pollution because of their toxic and non-biodegradable nature [24].

With the advancement in the field of nanotechnology, scientists have started the utilization of various plant products to synthesize nanocomposites. Nanocomposites are cost-effective, unharmful, and exhibit great antifungal properties. Plant-based nanocomposite has revealed better biocompatibility for biomedical applications in comparison to conventional chemical approaches [25,26]. Nowadays, further emphasis is being strained on raising efficient procedures to prepare nanocomposites [27]. Currently, the worth of bio-polymer-combined with ZnO nanocomposites has gained interest in the departments of biomedical, agriculture, and therapeutics due to their reliable and biodegradable properties [25,26]. For the synthesis of the nanocomposite, the ball-milling procedure is preferred over other techniques due to its solvent-lacking and environment-friendly, excellent yield, and economical [28]. The ball-milling procedure alters pure biochar by decreasing the particle size, increasing the surface area, enhancing the biochar functions, and creating reactive sites on the surface of biochar [29–31].

The present research has aimed to identify the pathogen of the leaf spot of Kiwi. For environment-friendly control of this disease, MB-ZnO nanocomposite has been synthesized through the ball-milled method and applied. Before antifungal activity analysis, synthesized nanoparticles have been characterized using ultra visible (UV) spectroscopy, Fourier transforms infrared (FTIR) spectroscopy, X-ray diffraction (XRD), thermo-gravitational analysis (TGA), scanning electron microscopy (SEM), and energy dispersive X-Ray (EDX) examination.

2. Materials and Methods

2.1. Field Observation

During October–November 2021, small brown spots were examined on the Kiwi leaves in the orchards of Islamabad's capital territory (33.6844° N, 73.0479° E) and neighboring areas (Figure 1). The samples of affected leaves were collected, labeled, and packed individually in sterile polythene bags and carried to the Molecular Plant Pathology laboratory for more assessment.
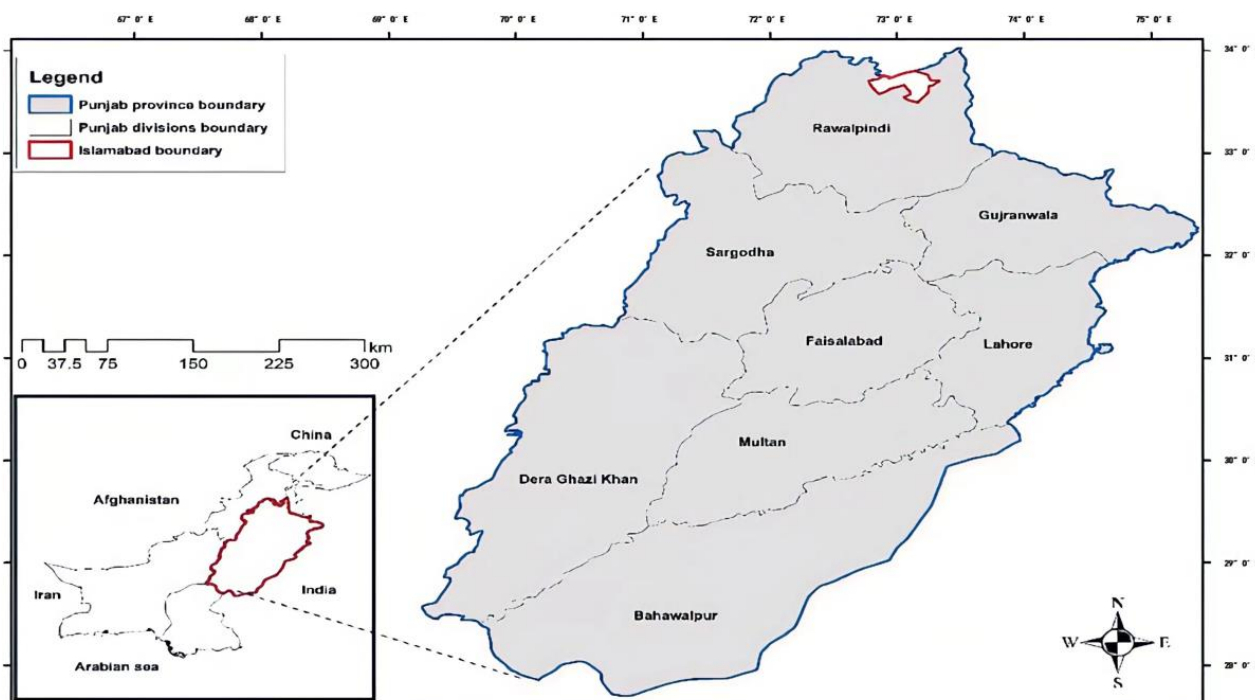
Figure 1. Sample collection area.

2.2. Isolation of Disease-Causing Agent from Infected Leaves

Surfaces of collected diseased leaves were treated with 75% ethanol and rinsed three times with autoclaved distilled H_2O. From each sterilized leaf, minor diseased portions (<1 cm^2) were excised and located on petri plates possessing potato dextrose agar (PDA). The petri plates were placed in an incubator at 28 °C for three days. After visible mycelial growth, single spore cultures were produced on PDA and incubated again. After one week of incubation, protrusive mycelial growth was examined and photographed from both the front and back sides of the petri plates.

2.3. Microscopic Recognition

For light microscopy, 1 to 2 droplets of lactophenol blue were positioned on the slide and from the edges of the fungus growth medium. Mycelial fragments were transferred to the slide. Mycelia were torn apart swiftly, and a drop of lactic acid was positioned on the slide. The coverslip was placed cautiously to evade bubbles, and the slide was examined with a microscope with a magnification of 40X.

2.4. Molecular Identification

Since all the isolates exhibited identical morphology, only a single isolate was arbitrarily selected and utilized for further pathogenicity tests and molecular identification. For genomic analysis, DNA was isolated using the standard CTAB method [32]. Concisely, for DNA isolation, 100 mM Tris-HCl pH 8, 2% CTAB, 1.4 M NaCl, 20 mM EDTA, and 1% PVP was applied. Forward ITS1 primer (FTCCGTAGGTGAACCTGCGG) and reverse ITS4 primer (TCCTCCGCTTATTGATATGC) were used to amplify partial ITS regions [33]. Briefly, the reactions were performed in 0.2-mL tubes in 100 μL reaction volume, comprising the following constituents: 10 mM Tris-HCl, 200 μM dNTP, 2.5 mM MgCl$_2$, 0.02 U/μL Taq DNA polymerase, 1 pmol/μL of each oligonucleotide primer, and 1 ng/μL genomic DNA template. Moreover, forward EF1 primer (GTTGTCATCGGTCACGTCGATTC) and reverse EF2 primer (ATGACACCRACAGCGACGGTTTG) were used to amplify the elongation factor 1-alpha (EF-1α) gene sequence. A polymerase chain reaction (PCR) was executed in a volume of 25 μL comprised of 10 μL of master mix, 1 μL of DNA template, 10 mM of each forward and reverse primer, and 13 μL of sterilized distilled water. The reaction was imple-

mented at 94 °C for 3 min, with a total of 35 cycles of 94 °C for 30 s, 56 °C for 30 s, 72 °C for 1 min, and a final step of 72 °C for 7 min. Amplified PCR resultant was sequenced and subjected to a BLAST study in the NCBI database (https://blast.ncbi.nlm.nih.gov/Blast.cgi accessed on 15 December 2022).

2.5. Phylogenetic Analysis through MEGA 7.0

For the construction of the phylogenetic tree, nucleotide sequences were aligned using MEGA (version 7.0) [34]. The phylogenetic tree was constructed by the maximum composite procedure using 1000 bootstrap replications.

2.6. Pathogenicity Test

Koch's postulates were followed to validate the pathogenicity of the isolated pathogen. Twenty healthy leaves of Kiwi were detached and surface sterilized. Ten leaves were injected using 10 μL conidial suspension (10^6 conidia mL^{-1}) of isolated fungus after wounding. The other ten leaves were injected with autoclaved distilled water and designated as the control treatment. All leaves were incubated at 25–28 °C and 75–80% relative humidity. After the development of lesions, the pathogen was again isolated on PDA, the and fungal morphology was studied.

2.7. Preparation of MB-ZnO Nanocomposite

The chemicals utilized in this study (ZnO, HCl, and NaOH) were bought commercially. All the chemical solutions used in the experiment were prepared in distilled water. Maize straw was obtained from the field, chopped to 1–1.5 mm size, and used for the synthesis of biochar, following a standard protocol [35]. Briefly, chopped maize straw was shade dried, pieced, sieved, and loaded into 10 g crucibles for its placement in a vacuum furnace. The powder was heated up at 600 °C for 6 h in an anaerobic environment. The obtained biochar was passed through a sieve and used to form the nanocomposite. Biochar nanocomposite (MB-ZnO) was synthesized by mixing obtained biochar with ZnO in a ball-milling machine. Precisely, 6 g of each ZnO and MB (50:50 by weight) was transferred to a container of 500 mL containing agate spheres of 180 g (diameter of 6 mm) and located in a ball-milling machine. The ratio of balls to MB and ZnO was 15:1 (by weight). The mechanical milling was done for 72 h in a moisture-free environment.

2.8. Characterization of Nanocomposite

A scanning electron microscope (SEM, JEOLJSM 25910) was used to investigate the surface characteristics of the MB-ZnO. The elemental study was performed by dispersive energy-dispersive X-ray spectroscopy (EDX, UKINCA 200). A spectrophotometer (SPECTRUM, 65) was utilized to get the FT-IR spectra. The crystallinity of the nanocomposite was studied at 0–80° with the help of X-ray diffraction (XRD, Bruker, D8, Billerica, Massachusetts, United States). The optical properties of the nanocomposite were examined from 200 to 800 nm with the help of UV-Vis diffused reflectance spectroscopy.

2.9. In Vitro Antifungal Potential of MB-ZnO

Following the poisoned food method, the antifungal potential of the MB-ZnO nanocomposite was deceived. For the determination of the antifungal ability of MB-ZnO, PDA culture media was amended with different concentrations 6 mg/mL, 12 mg/mL, and 19 mg/mL) of the biochar-ZnO nanocomposite. With the help of a Cork borer, a 4 mm inoculum disc of *R. oryzae* was placed in the middle of the petri plates. PDA with no nanocomposite worked as the control. The injected petri dishes were placed in an incubator for one week at 26 ± 1 °C, and the growth inhibition was determined using the formula mentioned below.

$$\text{Growth Inhibition \%} = (C - T)/C \times 100 \tag{1}$$

where C shows the average mycelial growth in the control petri plates, and T indicates the average mycelial growth in the MB-ZnO-treated petri plates. The experiment was performed in triplicate.

3. Results and Discussion

3.1. Isolation and Identification of the Disease-Causing Pathogen

Brown spots were observed irregularly on the Kiwi leaves (Figure 2A). The size and quantity of the irregular spots progressively increased and turned dark brown. The disease-causing pathogen was successfully isolated from these leaves, with 84% isolation frequency. After 5–6 days of incubation, whitish mycelia were observed, which turned grayish black and appeared in net-like structures (Figure 2B). On the hind side of the petri dish, the colonies were dark brown in appearance (Figure 2C). The appearance, color, and growth configuration were identical to earlier reported characteristics of *R. oryzae* [36]. Microscopic observations also provided deep insight into the identification of the isolated pathogen. Sporangiophores were generally straight, and they were present in solitary as well as cluster form. They were brownish in color; their lengths ranged between 220 and 1100 μm, and the width range was between 7 and 12 μm (Figure 2D). The color of sporangia was dark brown, and they were globose to sub-globose in shape with a diameter from 70 to 170 μm (Figure 2D). Sporangiospores were brownish in color and were angular, un-septate, and/or scarcely septate (Figure 2D). These microscopic features confirmed the studied pathogen as *R. oryzae* [37].
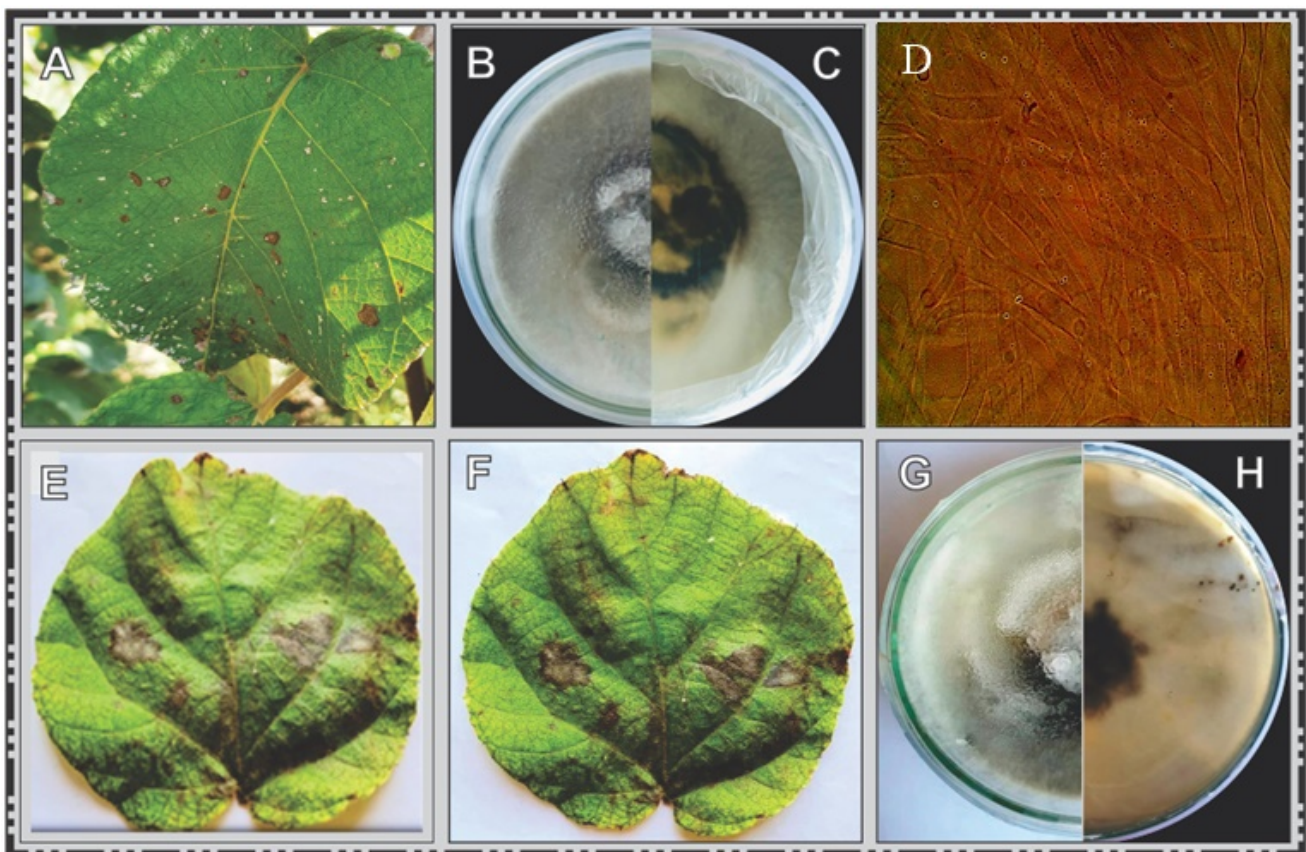

Figure 2. Leaf spots were observed on the leaves of Kiwi (**A**). The disease-causing fungus was grown in petri dishes and examined from the front side (**B**) and back side (**C**). Microscopic examination was done at 40× magnification (**D**). Healthy leaves were inoculated, and disease symptoms were examined after 3 days (**E**) and 5 days (**F**) of inoculation. The fungus was re-isolated and examined from the front (**G**) and back (**H**) sides of the petri dishes.

3.2. Pathogenicity Test

Inoculated healthy fruit exhibited grayish lesions after 3 days of inoculation (Figure 2E), which turned dark after 5 days (Figure 2F). On the control leaves, no lesion was developed, and they remained healthy. From these lesions, the pathogen (*R. oryzae*) was re-isolated on the PDA and showed similar mycelial morphology (Figure 2G,H). These findings confirmed the association of this fungus in the leaf spot of Kiwi.

3.3. Molecular Identification and Phylogenetic Analysis

To confirm the identity of *R. oryzae*, phylogenetic analysis of the representative isolates was carried out using genetic regions, ITS, and EF-1α. BLAST analysis of the resultant ITS1-ITS4 sequence showed > 99% resemblance with *R. oryzae* strain RAA internal transcribed spacer 1, partial sequence; 5.8S ribosomal RNA gene and internal transcribed spacer 2, complete sequence; and large subunit ribosomal RNA gene, partial sequence (MT603964.1), while EF-1α sequence revealed 100% similarity with *R. oryzae* translation elongation factor-1α gene (MK510718.1). The obtained ITS1-ITS4 sequence of *R. oryzae* was submitted to NCBI (MW603842.1). Phylogenetic analyses efficiently described the relationship between the amplified ITS1/ITS4 sequence (Figure 3) and EF-1α sequence (Figure 4), with closely related genes present in the NCBI database and verified BLAST analysis results.
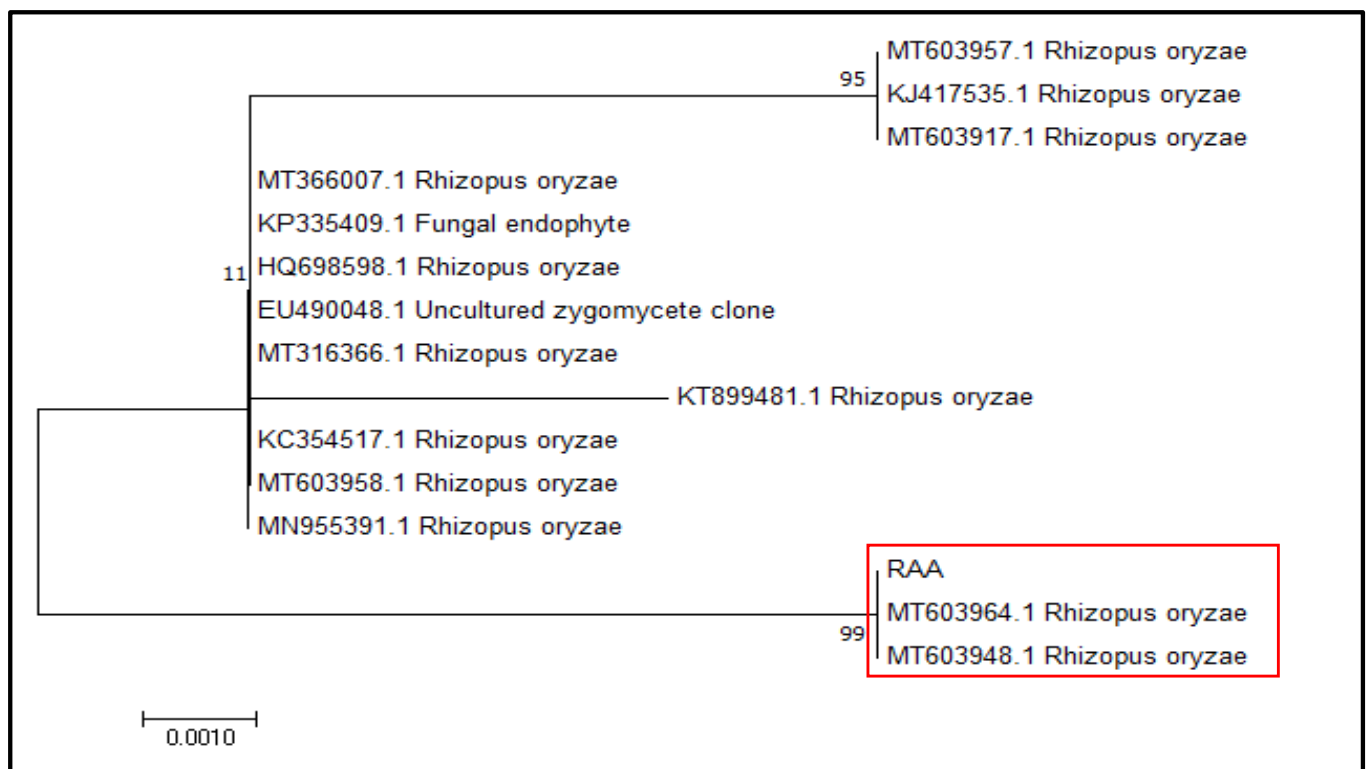

Figure 3. Phylogenetic study of the isolated *R. oryzae* sequence with 14 closely related ITS sequences after BLAST analysis. After 1000 replicates, the bootstrap values are presented at the branch points.
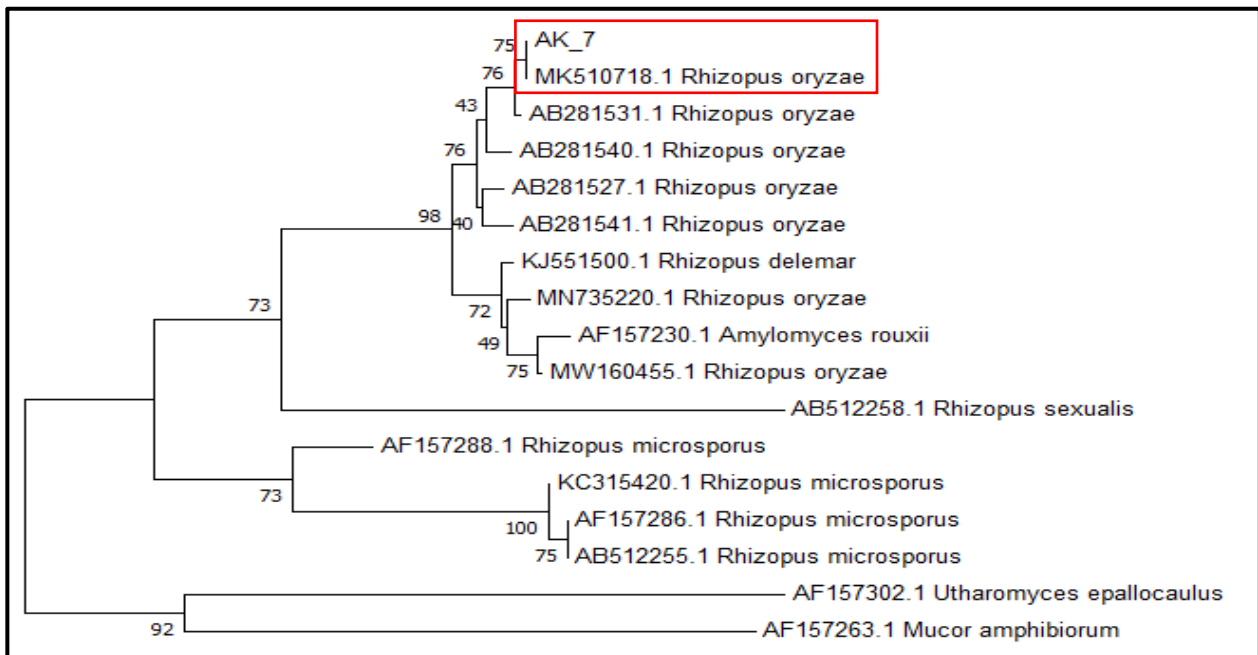
Figure 4. Phylogenetic study of the isolated *R. oryzae* sequence with 16 closely related EF-1α sequences after BLAST analysis. After 1000 replicates, the bootstrap values are presented at the branch points.

3.4. Depictions of MB-ZnO Nanocomposite

3.4.1. SEM and EDX Analyses

SEM assessments successfully studied the surface properties of pure, pristine biochar (Figure 5A) and MB-ZnO (Figure 5B). SEM images showed a rough and porous configuration of pure biochar. During the pyrolysis, biochar's rough and porous morphology was achieved through the vaporization of unstable materials. These structural properties of pristine biochar confirmed its proficiency to use as excellent support for nano-scale substances. After ball-milling, a white powdery substance (ZnO) showed on the biochar surface in a clustered form (Figure 5B). The SEM study revealed that the accumulation of raw materials on the biochar surface affects their textural properties along with the altered composition of products (Figure 5B). These observations confirm the successful formation of nanocomposites [38].
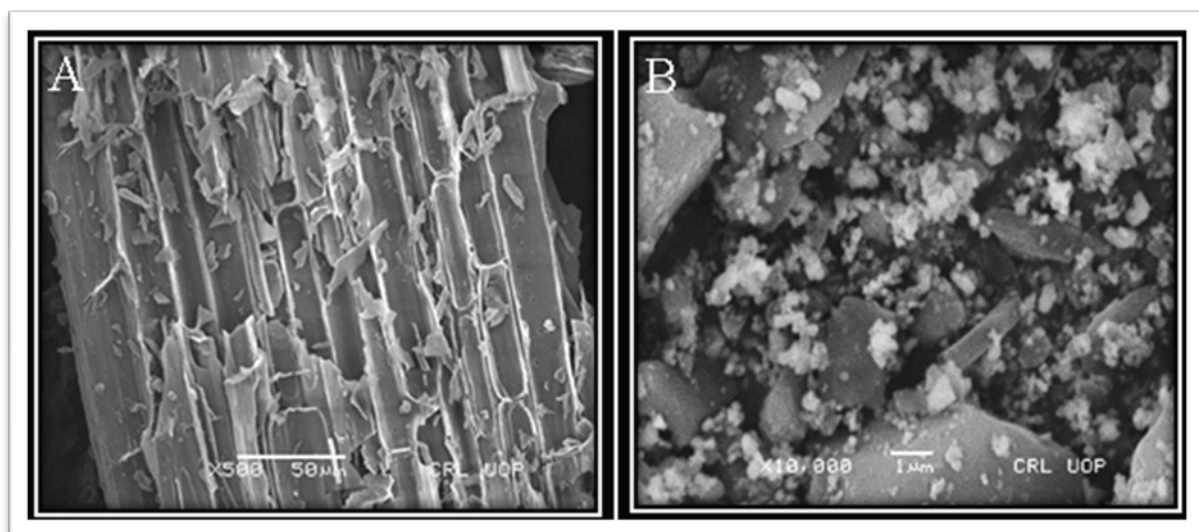

Figure 5. SEM micrographs of pristine MB (**A**) and MB-ZnO (**B**).

The elemental properties of MB-ZnO nanocomposite were found through EDX analysis, confirming the presence of C, O, Zn, Ca, Si, Na, P, and K elements on the MB-ZnO [39]. SEM and EDX studies of MB-ZnO nanocomposite confirmed the presence of ZnO on the biochar surface. These results are published by our team [39]. The EDX results are depicted in Figure 6.
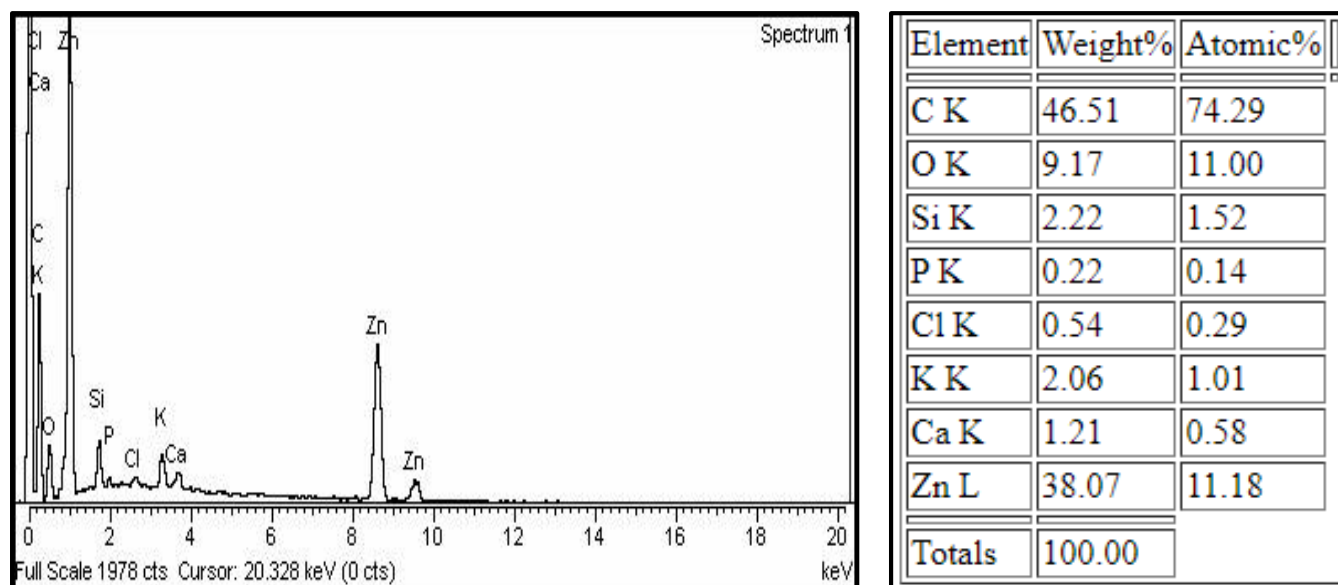

Element	Weight%	Atomic%
C K	46.51	74.29
O K	9.17	11.00
Si K	2.22	1.52
P K	0.22	0.14
Cl K	0.54	0.29
K K	2.06	1.01
Ca K	1.21	0.58
Zn L	38.07	11.18
Totals	100.00	

Figure 6. EDX graph (**left**) and elemental exploration of MB-ZnO nanocomposite (**right**).

3.4.2. XRD Analysis

The crystal structure of MB-ZnO was explored with a scanning rate of 1° per minute in 0.013° steps, encompassing a 2-θ angle from 10° to 70°. The XRD spectrum exposed nine key peaks of biochar nanocomposite (Figure 6). The diffraction peaks at 2-θ = 31.78, 34.43, 36.26, 47.55, 56.6, 62.9, 66.8, 67.9, 68.9, and 72.7° corresponded to the (100), (002), (101), (102), (110), (103), (200), (112), (201), (004), and (202) planes, individually [40]. MB-ZnO displayed the diffraction peaks indexed to hexagonal structure following the JCPDS no. (036-1451). The intense and short peak suggested no huge effect of the presence of carbon on the crystalline structure of ZnO [41]. The average normal size of the prepared MB-ZnO particle was calculated as 46 nm using an X-ray line broadening system [42].

3.4.3. FTIR Spectroscopy

FTIR analysis determined some characteristic functional groups on MB-ZnO (Figure 7). For MB-ZnO, relatively intense bands at 1650 and 3440 cm^{-1} described the bending vibration of H-O-H and O-H. Peaks at 2850 and 2940 cm^{-1} represented symmetric and asymmetric vibration modes of the C-H bond correspondingly [43]. Bands at 1037, 1124, 1325, 1417, and 1452 attributed to the stretching of Si-O-Si, C-H, C-C, CH_2 group, and COO^-, respectively [44,45]. Importantly, a durable peak at 524 cm^{-1} is credited to the stretching of Zn-O [46]. A superfluous peak at 580 cm^{-1} depicted Zn vibration and confirmed the presence of ZnO on the surface of the MB-ZnO. The complete FTIR spectra is shown in Figure 8.
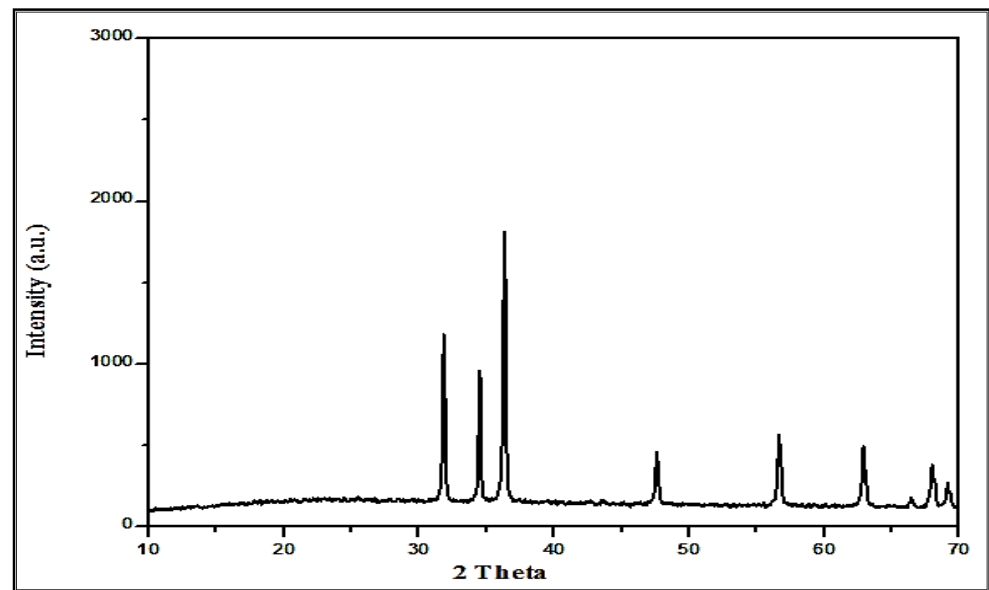
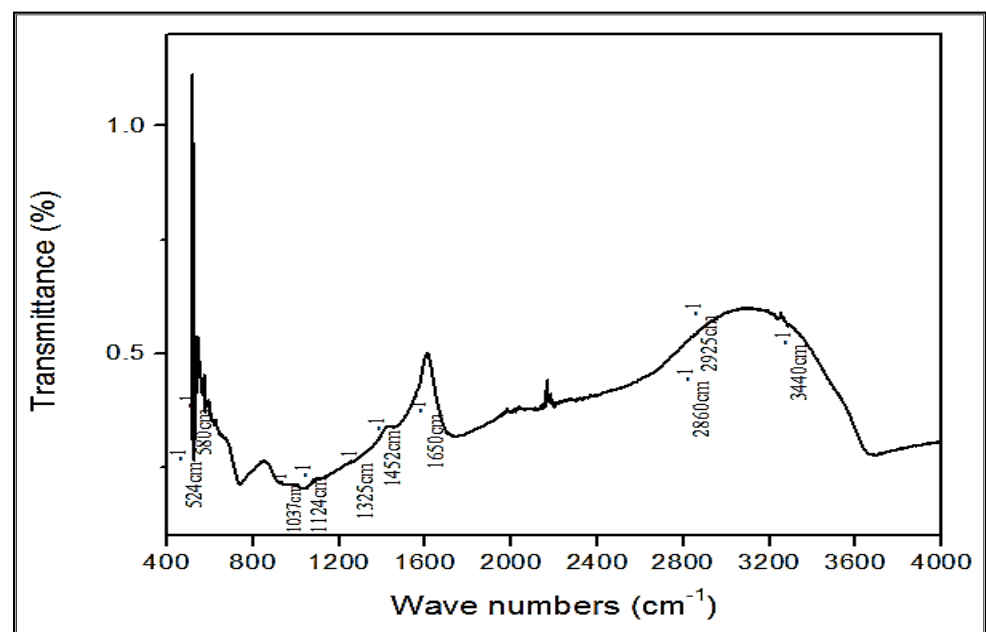**Figure 7.** XRD patterns of the MB-ZnO nanocomposite.

Figure 8. FTIR spectrum of the MB-ZnO nanocomposites.

3.4.4. VU Analysis

UV-vis absorption spectra of the pristine ZnO nanoparticles and MB-ZnO displayed sharp peaks ranging from 200 to 800 nm. Pure ZnO displayed strong absorption in the ultraviolet region (200–250 nm), while no peak was observed in the visible spectra, which is parallel with former studies [47]. The absorption peaks of MB-ZnO were assessed in the wavelength range from 250 to 320 nm. The difference in the peaks is accredited to the chemical interaction between the biochar and ZnO nanoparticles [48]. The UV spectra is shown in the Figure 9.
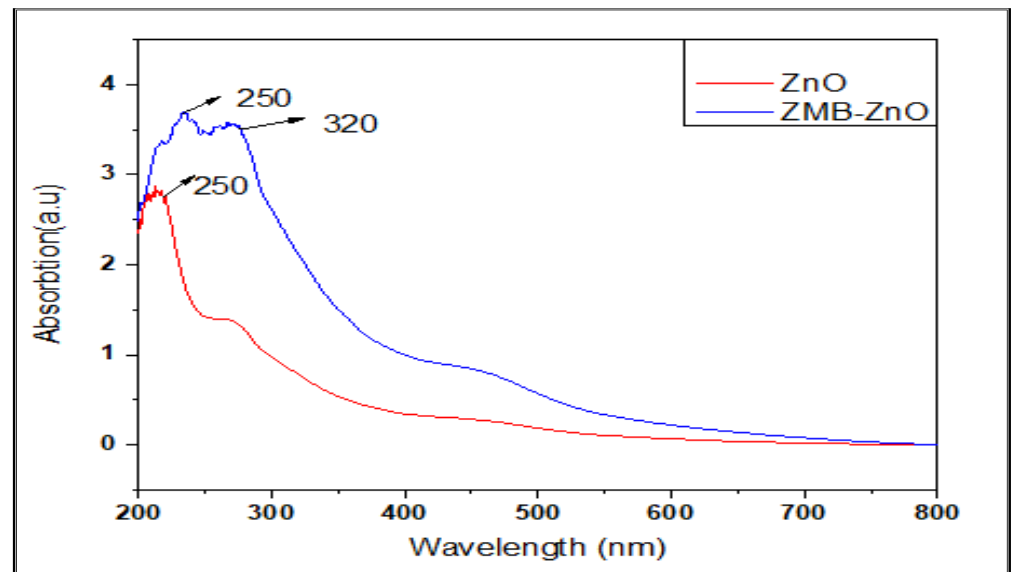
Figure 9. UV pattern of the ZnO and MB-ZnO.

3.4.5. Thermo Gravitational Analysis

TGA was performed to estimate the thermal properties of MB-ZnO. The findings of this exploration revealed good thermal properties of the ball-milled synthesized nanocomposite. This helps nanocomposite to perform under variable environmental stress conditions, and these results have been reported by our team previously [41].

3.5. Antifungal Activity Analysis

Variable mycelial inhibition was observed at different concentrations of the MB-ZnO nanocomposite on PDA media (Figure 10). A similar kind of fungal inhibition has been observed earlier [48]. The highest growth inhibition (79 ± 2.1%) was observed at 19 mg/mL dose rate (Figure 11), next was (67 ± 1.7%) at 12 mg/mL dosage, and (57.77 ± 0.5) at 6 mg/mL application rate. Additional escalation in the application rate of the MB-ZnO nanocomposite did not enhance growth inhibition, which might be due to rises in dosage resulting in the clustering of the MB-ZnO. Nanocomposite has a minor size but greater surface-to-volume ratios, making them greatly unstable and reactive [49]. The physio-chemical aspects, such as size, Brownian movement, and surface properties may also influence accumulation.

Figure 10. Effect of various concentrations of MB-ZnO on the growth of *R. oryzae.* (**A**) Control, (**B**) 19 mg/mL concentration, (**C**) 12 mg/mL concentration, (**D**) 6 mg/mL concentration.
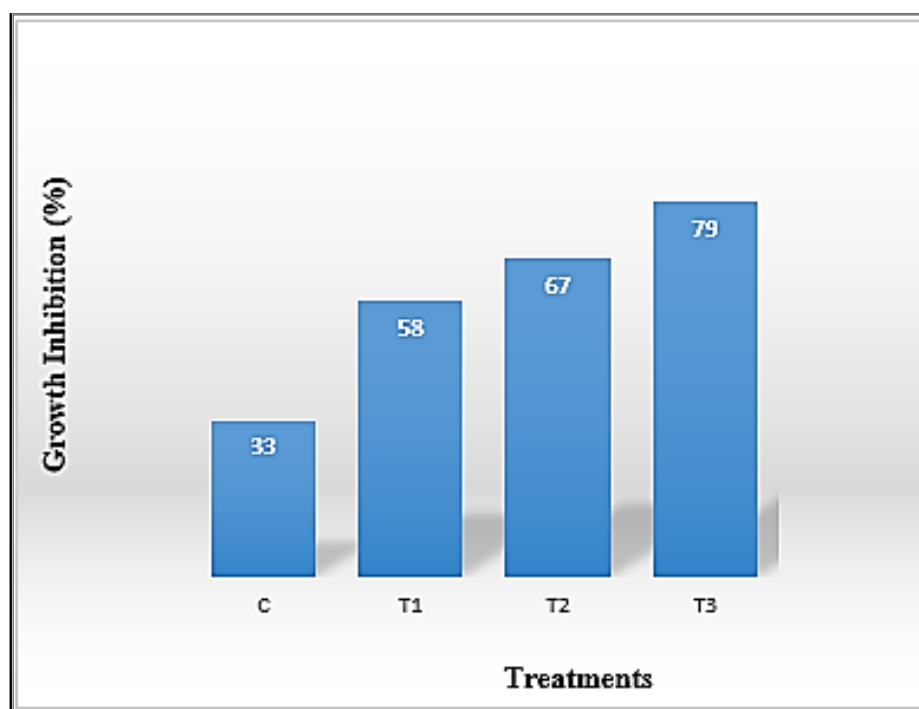
Figure 11. In vitro antifungal activity of MB-ZnO nanocomposite. C (control), T1 (6 mg/mL), T2 (12 mg/mL), and T3 (19 mg/mL).

A few years back, nanotechnologists effectually applied ZnO nanocomposite to inhibit the growth of different fungi, such as *Candida albicans*, *Botrytis cinerea*, *Pythium uttimum*, *Aspergillus niger*, and *Fusarium graminearum* [50–52]. Some researchers also propose that during microbial activity, ZnO nanoparticles generate Zn^{2+}, which damages the membrane of the pathogen [10]. The latest antimicrobial potential of metal-oxide nanoparticles consists of the production of poisonous ions to destroy cells [53]. It has been described that nano-sized particles strongly interact with the microbial surface and show antimicrobial activity [54]. Metals oxide nanocomposites create holes by breaking the cell wall and disturbing morphological characteristics of the cell membrane (permeability and polarity of the cell membranes and resulting in the cessation of the cell membrane and, therefore, without difficulty passing in the cell and causing the cessation of DNA, RNA, and proteins molecules in the cytoplasm of the cell [54]. This damage produces an outflow of various constituents, such as proteins, enzymes, RNA, and DNA and results in the death of a cell. Due to the large number of applications of *Actinidia chinensis,* different scientists used different methods to control the pathogens attacking Kiwi. Some other scientists used active ingredients of biological fungicides to control the Kiwi leaf spot [55].

From all these findings, it was concluded that this is the first study to report isolating *Rhizopus oryzae* from the Kiwi plant in Pakistan. MB-ZnO is an effective fungicide to control this novel pathogen.

4. Conclusions

In conclusion, it can be confirmed that *R. oryzae* is the disease-causing pathogen of the leaf spots on Kiwi. This is a novel study of *R. oryzae* causing leaf spot disease in Kiwi in Pakistan. In the present work, MB-ZnO was efficiently synthesized through an eco-friendly and price-effective procedure systematically elucidated above. The physicochemical characteristics were also investigated via different microscopic and spectroscopic techniques. The small size and different functional groups of the MB-ZnO nanocomposite were confirmed through FTIR and XRD studies and declared as effective antimicrobial agents. The XRD results showed that the ball-milled synthesized nanocomposite was in a crystalline shape, such as chemically synthesized pure ZnO. SEM and EDX results also confirmed

the agglutination of ZnO on the biochar surface. The current study also demonstrated the successful application of the MB-ZnO nanocomposite to control this disease. Because of its health-friendly composition, this nanocomposite can be sprayed on vegetables and fruits as an antifungal agent to replace harmful chemical fungicides.

Author Contributions: Conceptualization, A.K., M.F.H.M. and M.A.; methodology, A.K., M.F.H.M. and M.K.; software, A.K., D.A.A.F. and E.M.A.-Z.; validation, A.K., E.M.A.-Z. and M.F.H.M.; formal analysis, A.K. and M.A.; investigation and resources, M.F.H.M.; data curation, R.A.A. and M.S.E.; writing—original draft preparation, A.K. and M.F.H.M.; writing—review and editing, M.S.E., R.A.A., D.A.A.F. and E.M.A.-Z.; visualization, M.K., M.A. and A.K.; supervision and project administration, M.F.H.M. All authors have read and agreed to the published version of the manuscript.

References

1. Barboni, T.; Cannac, M.; Chiaramonti, N. Effect of cold storage and ozone treatment on physicochemical parameters, soluble sugars and organic acids in Actinidia deliciosa. *Food Chem.* **2010**, *121*, 946–951. [CrossRef]
2. The Kiwi Fruit in the World. Available online: http://areflh.org/en/francais/the-kiwi-fruit-in-the-world (accessed on 6 December 2022).
3. Afsharmanesh, H.; Ahmadzadeh, M.; Javan-Nikkhah, M.; Behboudi, K. Improvement in biocontrol activity of Bacillus subtilis UTB1 against Aspergillus flavus using gamma-irradiation. *Crop. Prot.* **2014**, *60*, 83–92. [CrossRef]
4. Teng, K.; Ruan, H.-S.; Zhang, H.-F. Flavonoid and saponin rich fractions of kiwi roots (Actinidia arguta (Sieb.et Zucc.) Planch) with antinociceptive and anti-inflammatory effects. *Afr. J. Pharm. Pharmacol.* **2013**, *7*, 2445–2451. [CrossRef]
5. Pinto, D.; Delerue-Matos, C.; Rodrigues, F. Bioactivity, phytochemical profile and pro-healthy properties of Actinidia arguta: A review. *Food Res. Int.* **2020**, *136*. [CrossRef]
6. Bayer, S.B.; Gearry, R.B.; Drummond, L.N. Putative mechanisms of kiwifruit on maintenance of normal gastrointestinal function. *Crit. Rev. Food Sci. Nutr.* **2018**, *58*, 2432–2452. [CrossRef]
7. Kvesitadze, G.I.; Kalandiya, A.G.; Papunidze, S.G.; Vanidze, M.R. Identification and Quantification of Ascorbic Acid in Kiwi Fruit by High-Performance Liquid Chromatography. *Appl. Biochem. Microbiol.* **2001**, *37*, 215–218. [CrossRef]
8. He, X.; Fang, J.; Chen, X.; Zhao, Z.; Li, Y.; Meng, Y.; Huang, L. Actinidia chinensis Planch.: A Review of Chemistry and Pharmacology. *Front. Pharmacol.* **2019**, *10*. [CrossRef]
9. Li, J.; Li, Y.; Wu, H.; Naraginti, S.; Wu, Y. Facile synthesis of ZnO nanoparticles by Actinidia deliciosa fruit peel extract: Bactericidal, anticancer and detoxification properties. *Environ. Res.* **2021**, *200*, 111433. [CrossRef]
10. Naraginti, S.; Li, Y. Preliminary investigation of catalytic, antioxidant, anticancer and bactericidal activity of green synthesized silver and gold nanoparticles using Actinidia deliciosa. *J. Photochem. Photobiol. B Biol.* **2017**, *170*, 225–234. [CrossRef]
11. Schipper, M.A. Revision of the genus Rhizopus. *Stud. Mycol.* **1984**, *25*, 1–34.
12. Stalpers, J.A. A revision of the genus Rhizopus II. The Rh. microsporus-group. *Stud. Mycol.* **1984**, *25*, 20–34.
13. Zheng, R.-Y. A monograph of Rhizopus. *Sydowia* **2007**, *59*, 273.
14. Liu, X.Y.; Huang, H.; Zheng, R.Y. Molecular phylogenetic relationships within Rhizopus based on combined analyses of ITS rDNA and pyrG gene sequences. *Sydowia* **2007**, *59*, 235.
15. Abe, A.; Asano, K.; Sone, T. A Molecular Phylogeny-Based Taxonomy of the Genus *Rhizopus*. *Biosci. Biotechnol. Biochem.* **2010**, *74*, 1325–1331. [CrossRef]
16. Battaglia, E.; Benoit, I.; Brink, J.V.D.; Wiebenga, A.; Coutinho, P.M.; Henrissat, B.; De Vries, R.P. Carbohydrate-active enzymes from the zygomycete fungus Rhizopus oryzae: A highly specialized approach to carbohydrate degradation depicted at genome level. *BMC Genom.* **2011**, *12*, 38. [CrossRef]
17. Lanoiselet, V.; Cother, E.; Ash, G. Aggregate sheath spot and sheath spot of rice. *Crop. Prot.* **2007**, *26*, 799–808. [CrossRef]
18. Naz, H.; Gul, S.; Chaudhary, H.; Munis, M. First report of rhizopus oryzae causing fruit rot of citrus medica L. *J. Plant Pathol.* **2015**, *1*, 215. (In Pakistan) [CrossRef]
19. Wang, R.Y.; Gao, B.; Chen, S.L.; Ma, J.; Li, X.H.; Xue, C.X. First Report of *Rhizopus oryzae* Causing Soft Rot on Storage Roots of Sweetpotato in China. *Plant Dis.* **2017**, *101*, 1039. [CrossRef]
20. Arif, S.; Liaquat, F.; Khizar, M.; Shah, I.H.; Inam, W.; Chaudhary, H.J.; Farooq, A.B.U.; Munis, M.F.H. First report of *Rhizopus oryzae* causing fruit rot of yellow oleander in Pakistan. *Can. J. Plant Pathol.* **2017**, *39*, 361–364. [CrossRef]

21. Arif, S.; Munis, M.F.; Liaquat, F.; Shah, I.; Zhang, Y. Leaf rot caused by Rhizopus oryzae on pak choy (Brassica campestris ssp. chinensis) in China. *Phytopathol. Mediter.* **2019**, *58*, 213–217. [CrossRef]

22. Kwon, J.-H.; Kang, D.-W.; Ha, J.-S.; Kim, J.-W.; Kwak, Y.-S. Soft Rot on Peach Caused by Rhizopus oryzae in Korea. *Korean J. Mycol.* **2012**, *40*, 65–68. [CrossRef]

23. Youssef, K.; Sanzani, S.M.; Ligorio, A.; Ippolito, A.; Terry, L.A. Sodium carbonate and bicarbonate treatments induce resistance to postharvest green mould on citrus fruit. *Postharvest Biol. Technol.* **2014**, *87*, 61–69. [CrossRef]

24. Zubrod, J.P.; Bundschuh, M.; Arts, G.; Brühl, C.A.; Imfeld, G.; Knäbel, A.; Smalling, K. Fungicides: An overlooked pesticide class? *Environmen. Sci. Technol.* **2019**, *53*, 3347–3365. [CrossRef] [PubMed]

25. Din, M.I.; Nabi, A.G.; Rani, A.; Aihetasham, A.; Mukhtar, M. Single step green synthesis of stable nickel and nickel oxide nanoparticles from Calotropis gigantea: Catalytic and antimicrobial potentials. *Environ. Nanotechnol. Monit. Manag.* **2018**, *9*, 29–36. [CrossRef]

26. Iravani, S. Green synthesis of metal nanoparticles using plants. *Green Chem.* **2011**, *13*, 2638–2650. [CrossRef]

27. Yuliarto, B.; Septiani, N.L.W.; Kaneti, Y.V.; Iqbal, M.; Gumilar, G.; Kim, M.; Na, J.; Wu, K.C.-W.; Yamauchi, Y. Green synthesis of metal oxide nanostructures using naturally occurring compounds for energy, environmental, and bio-related applications. *New J. Chem.* **2019**, *43*, 15846–15856. [CrossRef]

28. Ambika, S.; Sundararajan, M. Antibacterial behaviour of Vitex negundo extract assisted ZnO nanoparticles against pathogenic bacteria. *J. Photochem. Photobiol.* **2015**, *14*, 52–57. [CrossRef]

29. Jeong, G.H.; Lee, Y.W.; Kim, M.; Han, S.W. High-yield synthesis of multi-branched gold nanoparticles and their surface-enhanced Raman scattering properties. *J. Colloid Interface Sci.* **2008**, *329*, 97–102. [CrossRef]

30. Devatha, C.P.; Jagadeesh, K.; Patil, M. Effect of green synthesized iron nanoparticles by Azardirachta indica in different proportions on antibacterial activity. *Environ. Nanotechnol. Monitor. Manag.* **2018**, *9*, 85–94. [CrossRef]

31. Devatha, C.P.; Thalla, A.K.; Katte, S.Y. Green synthesis of iron nanoparticles using different leaf extracts for treatment of domestic wastewater. *J. Clean. Prod.* **2016**, *139*, 1425–1435. [CrossRef]

32. Cullings, K. Design and testing of a plant-specific PCR primer for ecological and evolutionary studies. *Mol. Ecol.* **1992**, *1*, 233–240. [CrossRef]

33. White, T.J.; Bruns, T.; Lee, S.; Taylor, J. Amplification and direct sequencing of fungal ribosomal RNA genes for phylogenetics. *Mycologia* **1990**, *18*, 315–322.

34. Kumar, M.; Xiong, X.; Wan, Z.; Sun, Y.; Tsang, D.C.; Gupta, J.; Gao, B.; Cao, X.; Tang, J.; Ok, Y.S. Ball milling as a mechanochemical technology for fabrication of novel biochar nanomaterials. *Bioresour. Technol.* **2020**, *312*, 123613. [CrossRef] [PubMed]

35. Zhang, X.; Yao, Z.; Zhao, S.; Xie, H.; Yang, M. Rhizopus Stem Rot of Orobanche aegyptiaca caused by Rhizopus oryzae in China. *J. Phytopathol.* **2013**, *161*, 745–748. [CrossRef]

36. Park, J.-H.; Cho, S.-E.; Kim, B.-S.; Shin, H.-D. First report of postharvest root rot caused by Rhizopus oryzae on Codonopsis lanceolata. *Australas. Plant Dis. Notes* **2014**, *9*. [CrossRef]

37. Tu, C.; Wei, J.; Guan, F.; Liu, Y.; Sun, Y.; Luo, Y. Biochar and bacteria inoculated biochar enhanced Cd and Cu immobilization and enzymatic activity in a polluted soil. *Environ. Int.* **2020**, *137*, 105576. [CrossRef]

38. Kamal, A.; Saleem, M.H.; Alshaya, H.; Okla, M.K.; Chaudhary, H.J.; Munis, M.F.H. Ball-milled synthesis of maize biochar-ZnO nanocomposite (MB-ZnO) and estimation of its photocatalyticability against different organic and inorganic pollutants. *J. Sau. Chem. Soc.* **2022**, 101445. [CrossRef]

39. Duo, S.; Zhong, R.; Liu, Z.; Wang, J.; Liu, T.; Huang, C.; Wu, H. One-step hydrothermal synthesis of ZnO microflowers and their composition-/hollow nanorod-dependent wettability and photocatalytic property. *J. Phys. Chem. Solids* **2018**, *120*, 20–33. [CrossRef]

40. Kamal, A.; Haroon, U.; Manghwar, H.; Alamer, K.H.; Alsudays, I.M.; Althobaiti, A.T.; Iqbal, A.; Akbar, M.; Farhana; Anar, M.; et al. Biological Applications of Ball-Milled Synthesized Biochar-Zinc Oxide Nanocomposite Using *Zea mays* L. *Molecules* **2022**, *27*, 5333. [CrossRef]

41. Louren cco, M.A.; Zeng, J.; Jagdale, P.; Castellino, M.; Sacco, A.; Farkhondehfal, M.A.; Pirri, C.F. Biochar/Zinc Oxide Composites as Effective Catalysts for Electrochemical CO2 Reduction. *Sustain. Chem. Eng.* **2021**, 5445–5453. [CrossRef]

42. Chu, C.-C.; White, K.L.; Liu, P.; Zhang, X.; Sue, H.-J. Electrical conductivity and thermal stability of polypropylene containing well-dispersed multi-walled carbon nanotubes disentangled with exfoliated nanoplatelets. *Carbon* **2012**, *50*, 4711–4721. [CrossRef]

43. Jung, K.-W.; Choi, B.H.; Dao, C.M.; Lee, Y.J.; Choi, J.-W.; Ahn, K.-H.; Lee, S.-H. Aluminum carboxylate-based metal organic frameworks for effective adsorption of anionic azo dyes from aqueous media. *J. Ind. Eng. Chem.* **2018**, *59*, 149–159. [CrossRef]

44. Saleh, T.A.; Adio, S.O.; Asif, M.; Dafalla, H. Statistical analysis of phenols adsorption on diethylenetriamine-modified activated carbon. *J. Clean. Prod.* **2018**, *182*, 960–968. [CrossRef]

45. Batra, N.; Tomar, M.; Gupta, V. Realization of an efficient cholesterol biosensor using ZnO nanostructured thin film. *Analyst* **2012**, *137*, 5854–5859. [CrossRef]

46. Monticone, S.; Tufeu, R.; Kanaev, A.V. Complex Nature of the UV and Visible Fluorescence of Colloidal ZnO Nanoparticles. *J. Phys. Chem. B* **1998**, *102*, 2854–2862. [CrossRef]

47. Akir, S.; Hamdi, A.; Addad, A.; Coffinier, Y.; Boukherroub, R.; Dakhlaoui Omrani, A. Facile synthesis of carbon-ZnO nanocomposite with enhanced visible light photocatalytic performance. *Appl. Surf. Sci.* **2017**, *400*, 461.e70. [CrossRef]

48. Bakr, A.; Sayed, N.; Salama, T.; Ali, I.O.; Gayed, R.; Negm, N. Potential of Mg–Zn–Al layered double hydroxide (LDH)/m ontmorillonite nanocomposite in remediation of wastewater containing manganese ions. *Res. Chem. Int.* **2018**, *44*, 389–405. [CrossRef]
49. Zhang, L.-J.; Yang, M.-Y.; Sun, Z.-H.; Tan, C.-X.; Weng, J.-Q.; Wu, H.-K.; Liu, X.-H. Synthesis and Antifungal Activity of 1,3,4-Thiadiazole Derivatives Containing Pyridine Group. *Lett. Drug Des. Discov.* **2014**, *11*, 1107–1111. [CrossRef]
50. Hoseinzadeh, A.; Habibi-Yangjeh, A.; Davari, M. Antifungal activity of magnetically separable Fe3O4/ZnO/AgBr nanocomposites prepared by a facile microwave-assisted method. *Prog. Nat. Sci. Mat. Int.* **2016**, *26*, 334–340. [CrossRef]
51. Omar, K.; Meena, B.I.; Muhammed, S.A. Study on the activity of ZnO-SnO2 nanocomposite against bacteria and fungi. *Physicochem. Probl. Miner. Process.* **2016**, *52*.
52. Thaya, R.; Malaikozhundan, B.; Vijayakumar, S.; Sivakamavalli, J.; Jeyasekar, R.; Shanthi, S.; Vaseeharan, B.; Ramasamy, P.; Sonawane, A. Chitosan coated Ag/ZnO nanocomposite and their antibiofilm, antifungal and cytotoxic effects on murine macrophages. *Microb. Pathog.* **2016**, *100*, 124–132. [CrossRef] [PubMed]
53. Nguyen, V.T.; Vu, V.T.; Nguyen, T.A.; Tran, V.K.; Nguyen-Tri, P. Antibacterial activity of TiO2-and ZnO-decorated with silver nanoparticles. *J. Compos. Sci.* **2019**, *3*, 61. [CrossRef]
54. Pereira, L.; Dias, N.; Carvalho, J.; Fernandes, S.; Santos, C.; Lima, N. Synthesis, characterization, and antifungal activity of chemically and fungal-produced silver nanoparticles against Trichophyton rubrum. *J. Appl. Microbiol.* **2014**, *117*, 1601–1613. [CrossRef] [PubMed]
55. Chen, J.; Ran, F.; Shi, J.; Chen, T.; Zhao, Z.; Zhang, Z.; He, L.; Li, W.; Wang, B.; Chen, X.; et al. Identification of the Causal Agent of Brown Leaf Spot on Kiwifruit and Its Sensitivity to Different Active Ingredients of Biological Fungicides. *Pathogens* **2022**, *11*, 673. [CrossRef]